Rational Structure Optimized Hybrid Nanogenerator for Highly Efficient Water Wave Energy Harvesting

Jiyu Wang, Lun Pan, Hengyu Guo, Binbin Zhang, Rongrong Zhang, Zhiyi Wu, Changsheng Wu, Lijun Yang, Ruijin Liao,* and Zhong Lin Wang*

Water wave energy is a promising renewable energy source that may alleviate the rising concerns over current resource depletion, but it is rarely exploited due to the lack of efficient energy harvesting technologies. In this work, a hybrid system with a triboelectric nanogenerator (TENG) and an electromagnetic generator (EMG) based on an optimized inner topological structure is reported to effectively harvest water wave energy. The TENG with etched polytetrafluoroethylene films and Cu electrodes utilizing the contact-freestanding mode is designed into a cubic structure, in which the EMG is well hybridized. An integration of TENG and EMG achieves mutual compensation of their own merits, enabling the hybrid system to deliver satisfactory output over a broad range of operation frequency. The output performance of TENG with varied inner topological structures is experimentally and theoretically compared, and a concept is proposed to further clarify the energy conversion efficiency, which should be considered in designing energy harvesting devices. The influences of oscillation frequency, amplitude, and dielectric materials on the output performance of the hybrid system are comprehensively studied on different platforms. Furthermore, the optimum operation frequency ranges for TENG and EMG are concluded. The proposed hybrid nanogenerator renders an effective approach toward large-scale blue energy harvesting over a broad frequency range.

1. Introduction

Ocean energy is regarded as a promising renewable and clean energy source to alleviate the rising concerns of resource depletion and threat of pollution.[1–3] Among the energy sources, water wave energy exhibits advantages of large power and wide distribution.[4,5] Without constructing large, heavy electromagnetic generators (EMGs) standing on the ocean floor or fixed to the sea bed, water wave energy provides one of the most feasible future technologies with lower operation cost and considerable power delivery.[4] However, it has been rarely exploited due to the lack of economical energy harvesting technologies.[6–8] The emergence of triboelectric nanogenerator (TENG) to harvest various types of ambient mechanical energy into electricity opens up a new field of energy conversion and application.[9–11] Different from the EMGs, the TENGs, driven by the Maxwell's displacement current, can effectively convert broadband frequency mechanical energy sources into electricity based on the coupling of triboelectrification and electrostatic induction.[12] Various TENGs have been demonstrated to harvest energy from a variety of sources,[13,14] such as vibrations,[15,16] human walking,[17,18] body motions,[19,20] water waves,[21–30] etc. With the flexible structure, maturing design, and abundant choice of materials, the TENGs exhibit unique merits of high voltage, high efficiency, low weight, and low fabrication cost. These features render the TENG to be a feasible technology to effectively harvest water wave energy in a broadband frequency.

Previously, most TENG prototypes have been designed into ball-shell structure that can float on/in the water following the natural oscillation.[25,26] However, such a structure, utilizing single-electrode[31,32] and attached-electrode modes,[33] cannot achieve favorable output power for the limitation by the electrostatic shield effect and the inadequate contact, respectively.[34] Moreover, other research works based upon the sliding mode[35] and the rolling-freestanding mode[22] TENGs are inevitably confronted with problems that the TENGs move and work simultaneously with the water waves, thus only little effective energy transmitted from waves to the inner device, resulting in a reduction of energy harvesting efficiency. Importantly, TENG

J. Wang, Prof. L. Pan, Dr. H. Guo, B. Zhang, Dr. Z. Wu, C. Wu, Prof. Z. L. Wang
School of Material Science and Engineering
Georgia Institute of Technology
Atlanta, GA 30332, USA
E-mail: zhong.wang@mse.gatech.edu
J. Wang, Prof. L. Yang, Prof. R. Liao
State Key Laboratory of Power Transmission Equipment
and System Security and New Technology
Chongqing University
Shapingba, Chongqing 400044, P. R. China
E-mail: rjliao@cqu.edu.cn
Prof. L. Pan, R. Zhang
Key Laboratory for Green Chemical Technology of Ministry of Education
School of Chemical Engineering and Technology
Tianjin University
Tianjin 300072, P. R. China
Prof. Z. L. Wang
Beijing Institute of Nanoenergy and Nanosystems
Chinese Academy of Sciences
Beijing 100083, P. R. China

The ORCID identification number(s) for the author(s) of this article can be found under https://doi.org/10.1002/aenm.201802892.

DOI: 10.1002/aenm.201802892

**ADVANCED
SCIENCE NEWS**
www.advancedsciencenews.com

**ADVANCED
ENERGY
MATERIALS**
www.advenergymat.de

should be further integrated with EMG to simultaneously and collaboratively harvest water wave energy.[36] In this way, TENG as capacitive-type generator suffers from a low output current with a relatively high output voltage, which can be compensated by the high output current produced by EMG. The EMG likewise has difficulties in effective energy conversion under low-frequency waves, which can be made up by TENG.[37] With the complementary output characteristics of TENG and EMG, the two outputs can be connected together on a same storage capacitor and the capacitor can concurrently store the powers from TENG and EMG effectively. Furthermore, the two outputs of the hybrid system can also be directly connected to different loads to supply power for different purposes, such as plasma discharge with TENG and power supply with EMG, through which both generators can harvest the energy with their best energy conversion pathways under only one external stimulus, which can largely enhance the overall energy conversion efficiency. In this regard, a feasible design of TENG that resolves aforementioned limitations should be formulated, and more importantly, a comprehensive strategy that appropriately hybridizes a TENG with an EMG should be proposed for blue energy harvesting.

In this work, a hybrid system with triboelectric nanogenerator and electromagnetic generator based on an optimized cubic structured unit is demonstrated for water wave harvesting. The TENG is designed into cubic structure and the contact-freestanding mode is utilized for water wave energy harvesting. By integrating the TENG and the EMG together, this complementary output performance enables the hybrid nanogenerator to deliver satisfactory output in a broad range of operation frequency. To increase the output performance of TENG, the devices with varied inner topological structures were experimentally compared. Based on the inner topological structure, we proposed a concept to further clarify the energy conversion efficiency, which can be regarded as a design factor for the energy harvesting device. Based on different platforms, the influences of oscillation frequency, amplitude, and dielectric materials were systematically studied. Furthermore, the optimum operation frequency ranges for TENG and EMG were concluded to obtain a full understanding of this hybrid system. This proposed device with flexible structure can be easily linked together to form a nanogenerator network, which provides an effective and sustainable way toward large-scale blue energy harvesting in the future.

2. Results and Discussion

As illustrated in **Figure 1**a, the hybrid system is designed in a double-wing structure, which consists of two coupled hybrid nanogenerator units and one pivot hinge as a center of the link. Each unit is supported on a bracket and then connected by two cantilever beams that are anchored on the bearing support in the pivot hinge. The pivot hinge is floated on water with polyfoam so that the nanogenerator operates parallel to the wave direction and effectively rides the waves.

The basic unit of hybrid nanogenerator consists of two parts, TENG and EMG, as schematically depicted in Figure 1b. The TENG is composed of two parts: an acrylic box and four

shakable boards. The acrylic box used as the shell of TENG is divided into four separate chambers by three acrylic clapboards, and the four shakable boards are separately placed in the chambers. One edge of the shakable board is fixed at the roof of each chamber by attached flexible films, making the board freestanding and allowing easy contact with the walls of chambers. The polytetrafluoroethylene (PTFE) film employed as the triboelectric material is covered on both sides of the shakable boards, while the Cu electrodes are anchored on the internal walls of each chamber. With such a structure, the PTFE film attached on the board can get in full contact with Cu electrodes alternately under wave oscillations. In addition, according to the contact status between the PTFE film and Cu electrodes under water oscillation, all of the electrodes in four chambers are grouped as two terminal electrodes in a parallel connection.

The EMG part mainly consists of two pairs of magnets and two pairs of copper coils. Each pair of magnets is embedded in the shakable block that belongs to one of the outermost chambers. Each pair of copper coils is installed on the outer walls of the chambers, with their centers aligned in line with the centers of the magnets, when the shakable board contacts with the walls of box. An alternative electromotive force is formed when the magnets are moved toward the coils or away from the coils. By designing adjacent magnets with the same magnetic polarizations and the adjacent coils with the same winding directions, all of the coils are connected in series with the induced voltage enhanced and the induced current unchanged. This is the key strategy to achieve a simultaneous operation of the TENG and EMG, and they can be fully isolated from the water environment by using the encapsulating acrylic shield. Figure 1c,d exhibits the photographs of the fabricated hybrid nanogenerator with the dimensions of 4.5 in. × 5 in. × 6.5 in. (detailed fabrication process is provided in the Experimental Section).

To increase the triboelectric charges and further improve the output performance of TENG, the surface roughnesses of both Cu electrodes and PTFE films were modified by the surface etching method. The electrochemical erosion with a constant current density was conducted to treat Cu electrodes under the electrodischarge platform. The scanning electron microscopy (SEM) images (Figure 1e,f) show that cubic nanoparticles (NPs) are uniformly formed on the surface of Cu films, and the X-ray diffraction (XRD) patterns (Figure S1a, Supporting Information) confirm that the cubic NPs are crystallized Cu_2O, which will significantly increase the surface contact area without affecting the electroconductivity. Meanwhile, the plasma etching method was applied to treat PTFE film, whose morphology was obtained by atomic force microscopy (AFM) characterizations (Figure 1g,h). The uniform protuberances are formed after treatment, leading to an obvious increase in the surface roughness (Figure S1b–d, Supporting Information). In addition, the Fourier transform infrared spectroscopy spectra (Figure S1e, Supporting Information) indicate that the plasma etching process only alters the surface morphology but does not cause the variation of surface chemical groups.

The working principle of the hybrid nanogenerator includes two parts: the TENG part and the EMG part (see **Figure 2**a). The operation of the TENG is based on coupling of contact triboelectrification and electrostatic induction, while the EMG
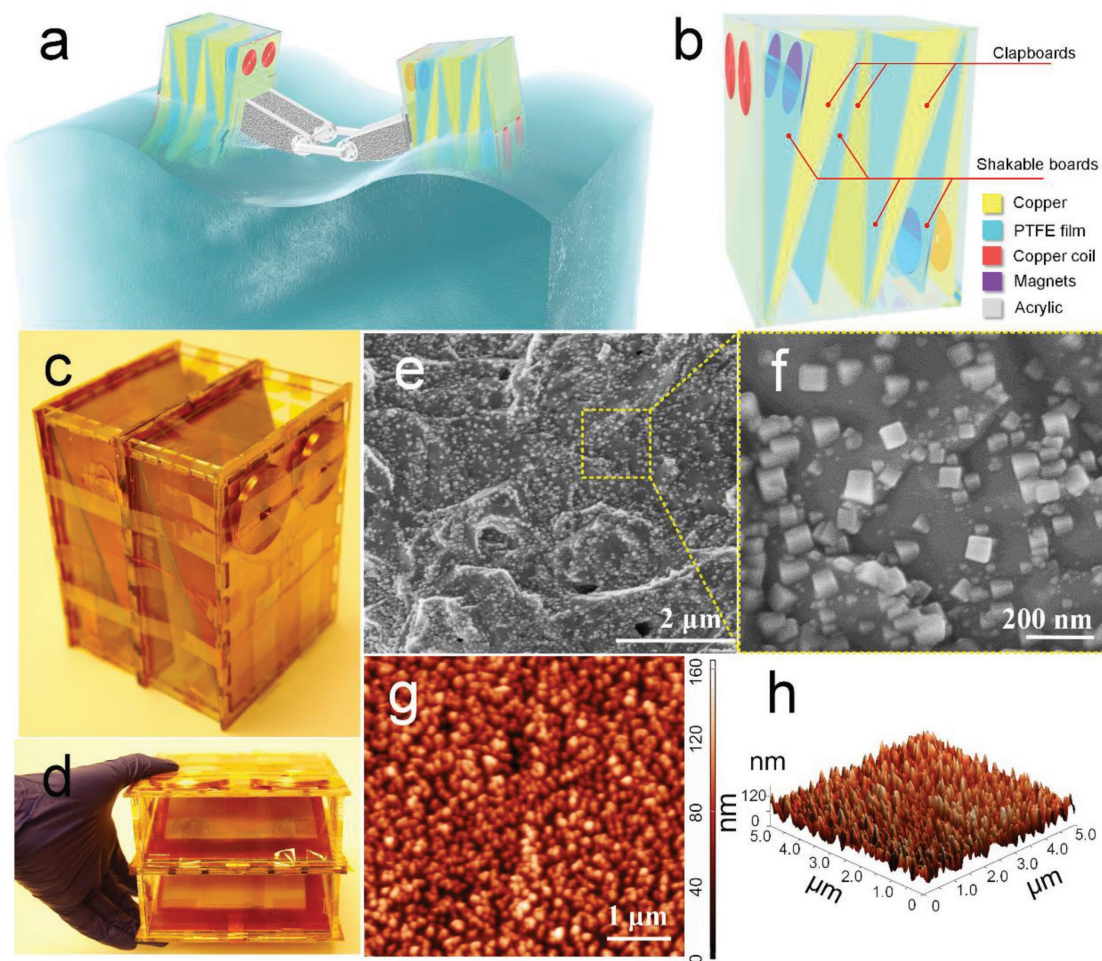
Figure 1. Structural design of ocean energy hybrid nanogenerator. a) Schematic illustration of the hybrid system with a double-wing structure riding on the water wave, which is basically constituted by b) a cubic structured unit hybridizing TENG and EMG. Photographs of c) as-fabricated hybrid nanogenerator and d) its vertical view. e,f) SEM images of the etched Cu electrode. g,h) AFM images of the etched PTFE film.

is based on Faraday's electromagnetic induction effect. At the initial stage, the full contact between PTFE board and Cu electrode creates equal amount of negative and positive charges on their surfaces, respectively (i). Then, triggered by external oscillation, the PTFE board begins to separate from the original Cu electrode and a potential difference establishes between two electrodes. The positive charges from the original electrode thus transfer to another Cu electrode via the load to rebalance electrostatic status (ii). The charge transfer continues during the whole process until another electrode is fully overlapped by PTFE board and a new equilibrium is established (iii), which is regarded as the first half cycle of TENG electricity generation. After that, PTFE board tends to move back to its original position due to external triggering; the positive charges transfer in the opposite direction by the reversed potential difference, with a reversed current subsequently formed in the load (iv). This is the second half of TENG electricity generation process. Simultaneously, the magnets embedded in PTFE board move toward or away from the coils to create output that is synchronized with that of TENG. Initially, there is no current output due to constant magnetic flux in the coil before the forward

movement of PTFE board (i). As the magnets start to move left with the PTFE board, the magnetic flux that crosses the coil increases and the induced current is generated in the coil to offset the increase of magnetic flux in the coil (ii). The current increases first and then decreases to zero as PTFE board reaches the overlapping position of the opposite electrode, due to the unchanged magnetic flux in the coil (iii). Similarly, the magnetic flux that crosses in the coil decreases during the back movement of PTFE board inducing a reverse current in the coil to compensate the decrease of magnetic flux (iv). The value of the reversed current also increases first and then decreases to zero at the end of complete cycle of EMG electricity generation process.

Furthermore, the charge distribution in the open-circuit condition is also illustrated at three particular positions, and the continuous variation of the open-circuit voltage (V_{oc}) is visualized through finite-element simulation using COMSOL (Figure 2b). The V_{oc} is then defined as the electric potential difference between the two electrodes. The electrostatic induction process can produce V_{oc} signal as the nonmobile triboelectric charges on PTFE film orderly screened by the positive
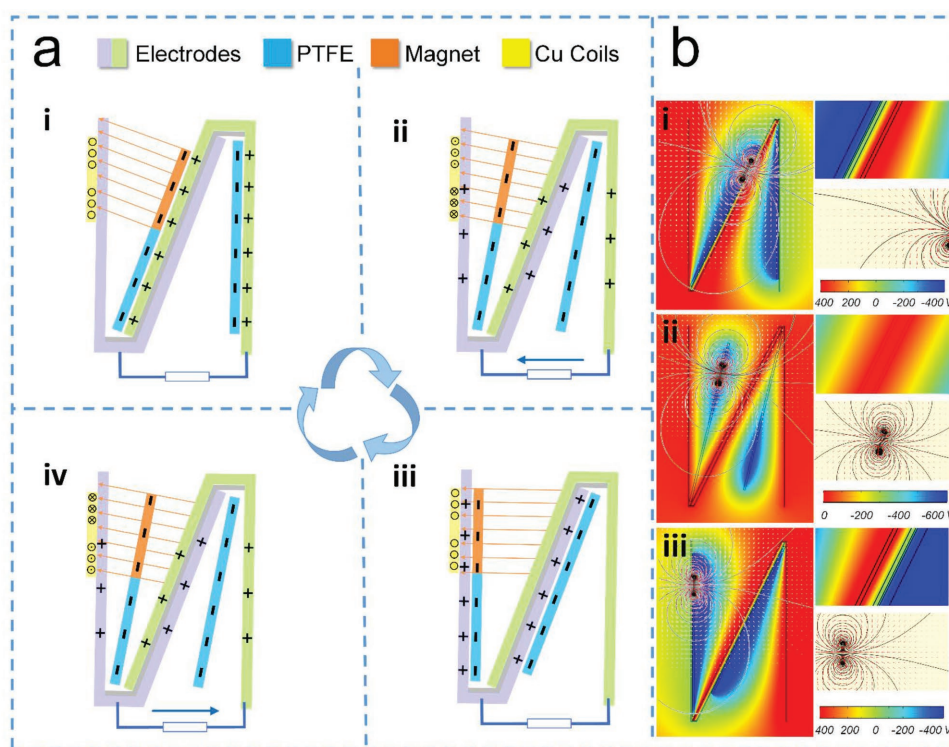
Figure 2. Schematics of working principle of the hybrid nanogenerator. a) Schematic of charge distribution and current direction of the hybridized TENG and EMG based on a half unit (i–iv). b) Electric potential distributions and magnetic flux at three typical displacements (i–iii) via COMSOL simulation. The local enlarged images on the right side show the electric potential distributions across two electrodes (top right), the magnetic flux distribution to the installed coil (middle right), and the color legend (bottom right).
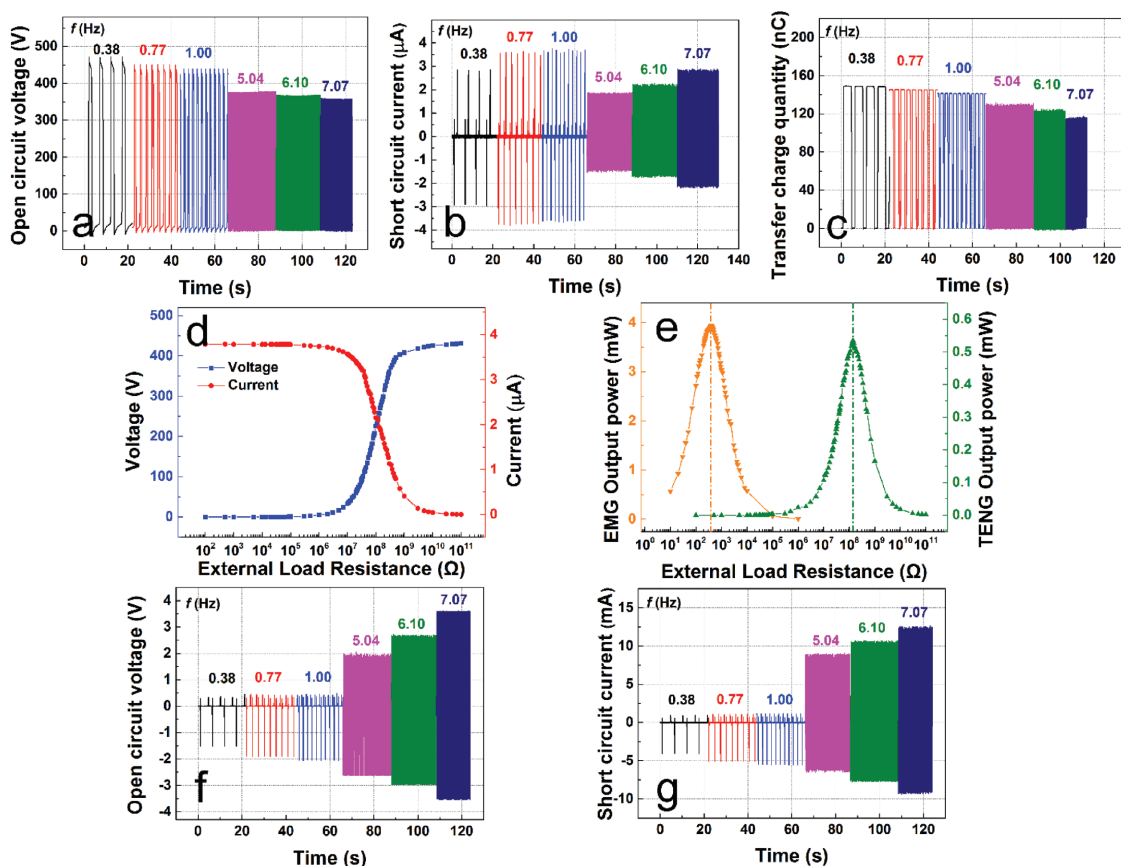
triboelectric charges on Cu electrode. Therefore, the maximum V_{oc} value appears at states (i) and (iii), when the negative charges are fully screened by the positive charges on one of the electrodes. Such a voltage then diminishes as PTFE board moves. Once the board passes the center position between two electrodes, the V_{oc} value reaches the zero-crossing point (ii, iv) and the V_{oc} with the opposite polarity starts to build up until the board moves back to this center position. Further reciprocating movement of PTFE board induces the V_{oc} to change in a reversed way because of the symmetric structure. In addition, the distribution of magnetic flux is also simulated in the three positions with results displayed in Figure 2b.

The operation of the hybrid nanogenerator under a broadband frequency was simulated by two platforms, of which the shaker platform was used to impose low-frequency (0.14–1 Hz) oscillations with adjustable amplitudes, while the linear motor platform was employed to simulate relatively high-frequency (4.91–7.07 Hz) horizontal shifting energy. The electrical output performances were tested for TENG and EMG at different frequencies under both platforms (Figure S2, Supporting Information), and the results at typical frequencies are shown in **Figure 3**a–e.

As demonstrated in Figure 3a–c, the peak value of V_{oc} for the TENG part decreases from 470 to 357 V and the peak value of Q_{sc} similarly varies from 150 to 120 nC with the frequency ranging from 0.38 to 7.70 Hz, exhibiting a slightly decreasing trend with the increase of frequency, which should be attributed to the reduction of effective contact area between the PTFE board and Cu electrodes. The peak value of V_{oc} occurs when the nonmobile negative charges on the PTFE board are fully screened by the positive charges on the electrode driven from the loop, requiring that the two surfaces of friction materials are fully contacted. Once the movement of PTFE board is accelerated by increasing oscillation frequency, the effective contact area is reduced because of the accordingly slight deformation of the surface. In this case, the positive charges are not completely driven from the loop to the surface of the electrode and fully screen the corresponding negative charges, resulting in the reduction of V_{oc} and Q_{sc}. This phenomenon would be magnified under the linear motor platform, where the effective contact area is further reduced because of only horizontal shifting, leading to a further decrease in both V_{oc} and Q_{sc}. In addition, the charge density ρ_{sc} can also be calculated as 1.31 nC cm^{-2} based on the known transfer charge quantity and the size of dielectric layer.

Conversely, the peak value of short-circuit current (I_{sc}) represents an increasing trend with the increasing frequencies, with the maximum peak value of 3.7 µA at a frequency of 1 Hz under the shaker platform, and the maximum peak value of 2.9 µA at a horizontal shifting frequency of 7.07 Hz. The output current is defined as the flow rate of charges. Although the transfer charges are slightly reduced, the flow rate of charges is largely increased under the increasing frequencies producing the increased current. Notably, the peak value of I_{sc} experiences a significant decrease when the platform switches from shaker to linear motor, which is a result of the reduced transfer charges.

**ADVANCED
SCIENCE NEWS**
www.advancedsciencenews.com

**ADVANCED
ENERGY
MATERIALS**
www.advenergymat.de

Figure 3. Electrical measurements of hybrid nanogenerator. a) V_{oc}, b) I_{sc}, and c) Q_{sc} of TENG under typical frequencies of 0.38, 0.77, 1.00, 5.04, 6.10, and 7.07 Hz. d) Output voltage and current of TENG under varied external load resistances. e) Dependence of output peak powers for both TENG and EMG on varied resistive loads. f) V_{oc} and g) I_{sc} of EMG under the same operation frequencies as TENG.

Once an external load is applied, the peak value of I_{sc} decreases as the load resistance increases, while the peak value of V_{oc} follows a reverse trend, as shown in Figure 3d. The instantaneous output power is maximized at a load resistance of ≈100 MΩ, corresponding to a peak power density of ≈0.5 mW at an operation frequency of 1 Hz (Figure 3e).

For EMG, both V_{oc} and I_{sc} are proportional to the whole operation frequency and increase from 1.5 to 2.8 V and from 4.0 to 12.5 mA, respectively, as shown in Figure 3f,g. The results are consistent with the Faraday's law, in which the electromotive force (V_{oc}) induced in a coil is proportional to time–rate variation of magnetic flux linkage through a coil and is given as follows

$$V_{oc} = -N\frac{d\Phi}{dt} \tag{1}$$

where Φ is the total magnetic flux linkage in one turn of the coil and N is the number of the coil's turns. Regarding the proposed EMG system that consists of a stationary coil and a movable magnet, the V_{oc} in the coil can be further expressed as

$$V_{oc} = -N\frac{d\Phi}{dt} = -NS\frac{dB(x)}{dt} = -NS\frac{dB(x)}{dx}\frac{dx}{dt} = -NS\frac{dB(x)}{dx}v \tag{2}$$

where $B(x)$ is the magnetic flux density through the coil, S is the area of the coil, and v is the velocity of the magnet. Once the coil is connected to an electrometer directly, the I_{sc} generated in the coil can be expressed as

$$I_{sc} = \frac{V_{oc}}{R_{coil}} = -\frac{NS}{R_{coil}}\frac{dB(x)}{dx}v \tag{3}$$

where R_{coil} is the internal resistance of the coil.

Based on Equations (2) and (3), both V_{oc} and I_{sc} show positive correlations with the velocity of the magnet, which is proportional to the oscillation frequency. The instantaneous output power of EMG is maximized at a load resistance of ≈100 Ω, corresponding to a peak power density of ≈4 mW, as shown in Figure 3e. The different matched load resistances between TENG and EMG can be attributed to the different types of internal impedances, of which the internal impedance of TENG is capacitive, while that of EMG is resistive. Furthermore, owing to the inherent features of TENG and EMG, these two generators exhibit different domains for not only load resistance but also operation frequency. The harvesting map of relative contribution by TENG and EMG to overall power with frequency and load resistance was plotted by measuring the dependence of output powers for both TENG and EMG on varied resistive loads under typical frequencies, as shown in Figure S3 in the

Supporting Information. Generally, the TENG dominates in the overall power under the condition of high resistance and low frequency, and EMG accounts for the main part under the condition of low resistance and high frequency. Since two domains share a very small overlapping region, the impact of one system normally plays relatively weak role in another one. Even if each one reaches the maximum output power point, the reduced output of another for the adverse interaction will not influence the overall output of system. In this regard, by integrating the TENG and the EMG together, the two generators can independently harvest energy by their own with a very slight and negligible mutual interaction. More importantly, both TENG and EMG can independently harvest energy on their own domains and mutually compensate each other, which can greatly expand the scope of application in a wide operation frequency and load resistance.

To increase the output performance of the hybrid nanogenerator, the device structure was initially optimized by exploring the output performances caused by changed inner topological structures. Considering the operation mode of TENG, the cubic device can be divided into several separated chambers shaped in triangular prism structure (**Figure 4**a; Figure S4, Supporting Information). Based on the fabricated devices with

changed inner topological structures, typical electric signals for both TENG and EMG were measured (Figure S5, Supporting Information). Specifically, V_{oc} of TENG decreases from 550 to 350 V with the increasing number of inner segments, while I_{sc} of TENG increases from 1.0 to 3.0 µA, exhibiting a reverse trend. The change of V_{oc} and I_{sc} generally confirms the principle of freestanding mode, in which the change of V_{oc} can be attributed to the variation of equivalent capacitor. The capacitor between two boards with fixed angle in single segment can be calculated as the plane-parallel capacitor mode, whose equivalent capacitor value exhibits reciprocal relationship to the angle. In this case, as the inner segments increase, the triboelectric charges on both boards remain almost the same, while the value of equivalent capacitor increases, leading to a decrease in V_{oc}, as for the I_{sc}, which is related to the transfer charge quantity and the flow rate of charges. With the increase of inner segments, the total triboelectric charge quantity linearly increases, and the flow rate of total charges increases as well due to the shorter swing distance. Therefore, the value of I_{sc} would be further increased. For the EMG, V_{oc} decreases with the increasing number of segments and I_{sc} shares a similar downtrend due to resistive impedance type of EMG. The output powers for both TENG and EMG are also obtained by connecting varied external
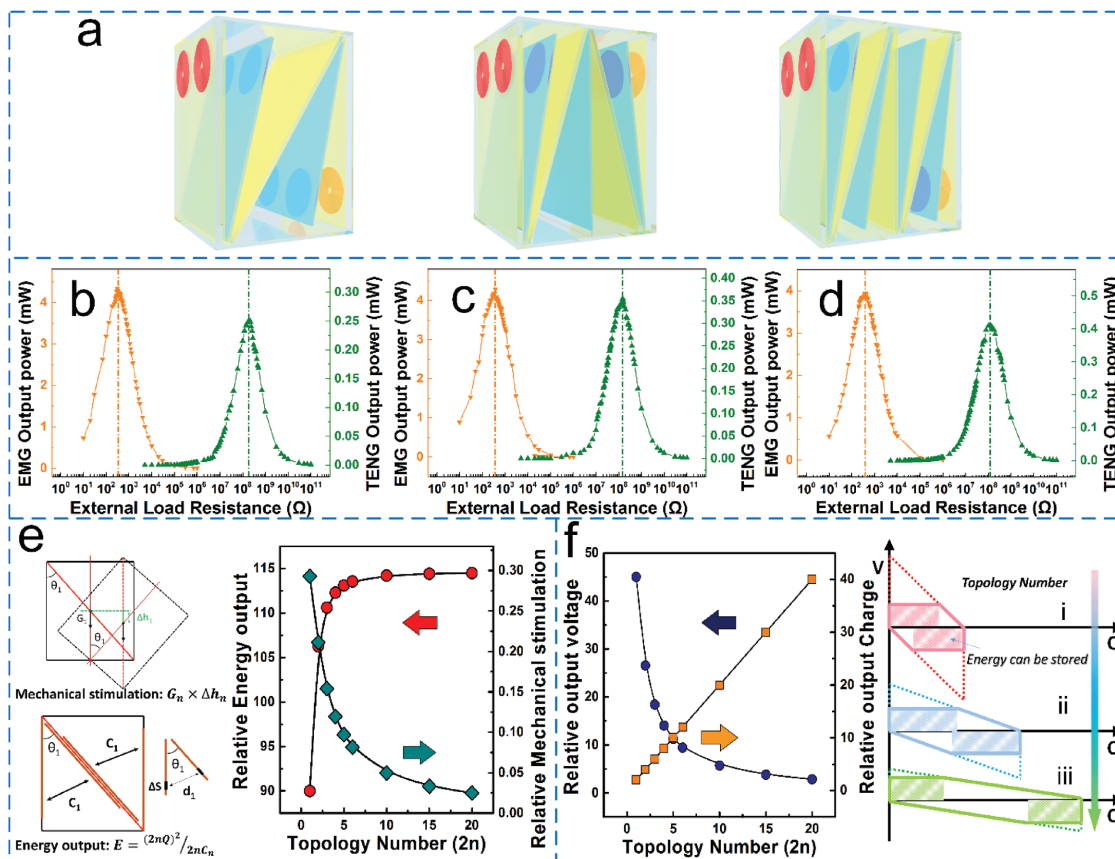
Figure 4. Inner topological structure that influences the energy utilization efficiency of the device. a) Schematic illustrations of hybrid nanogenerators with two, three, and four chambers. Dependence of output peak powers on varied resistive loads for the hybrid nanogenerators with b) two chambers, c) three chambers, and d) four chambers. e) Dependence of relative mechanical energy stimulated into the device and energy output tendency on the increasing topology number by theoretical derivation. f) Dependence of relative output voltage and output charges on the increasing topology number by theoretical derivation (left), and schematic diagram of V–Q curves with different topology numbers (right) (dash line shows the maximum energy that can be generated by the TENG device and shadow area represents the energy that can be utilized when using a constant external load).

1802892 (6 of 12)

ADVANCED
SCIENCE NEWS
www.advancedsciencenews.com

ADVANCED
ENERGY
MATERIALS
www.advenergymat.de

resistances (Figure 4b–d). The operating load ranges as well as the matched load resistances for TENG and EMG remain the same, while the maximum value of output power varies with different designs. Specifically, with the increasing number of inner chambers, the output power for EMG decreases with a decline rate of ≈7%, while the power for TENG increases with a growth rate of ≈60%, demonstrating that the inner topological structure exhibits a significant influence on the output performance of TENG, but less impact on that of EMG. Therefore, the effect of inner topological structure on the output performance of TENG was further explored.

The output performance of TENG used for energy harvesting can be normally regarded as the efficiency of energy conversion that converts the external mechanical energy into electric output. Herein, we initially proposed that the energy conversion can be further subdivided into two parts: the energy collected from external environment and the energy that can be stored. In this case, the energy conversion efficiency can be expressed as follows

$$\eta_{total} = \eta_{collect} \times \eta_{store} \tag{4}$$

where the energy conversion efficiency η_{total} is a combined result of the energy collection efficiency $\eta_{collect}$ and the energy storage efficiency η_{store}. The energy collection efficiency can be defined as

$$\eta_{collect} = \frac{E_{output}}{E_{input}} \tag{5}$$

where E_{input} is the required external mechanical stimulation and E_{output} is the maximum energy output it can provide, which all vary with the increasing inner topology number. As shown in the top left of Figure 4e, the angular displacement for the movable board decreases with the increasing number of segments; thus, the descending height for the center of gravity is reduced. As a result, less mechanical stimulation is required to achieve a complete contact–separation process for electricity generation. On the other hand, as shown in the bottom left of Figure 4e, the equivalent capacitor value increases as the spacing distance of electrodes reduces. Therefore, more triboelectric charges can be stored on the surfaces of electrodes to enhance the maximum energy output. As topology number largely increases, the relative mechanical stimulation and the relative energy output can be theoretically derived with the curves displayed in Figure 4e. The curve for the mechanical stimulation declines sharply and then gradually reaches a saturation value with the increasing topology number, while the curve for the energy output exhibits a reverse trend. The higher energy collection efficiency therefore can be achieved through the increased energy output and reduced mechanical stimulation by increasing the topology number. In addition, the mechanical stimulation can also be regarded as the threshold value of energy input for triggering the device operation, which should be considered in the energy harvesting field. For the harvesting device, a certain value of energy input is necessary to start the electricity generation. However, when the actual energy input is lower than the threshold value, the device cannot effectively harvest this external energy, leading to a waste of the energy. Although the external energy can be largely converted in the harvesting device, the converted energy cannot be fully stored because of the energy storage efficiency, which is expressed as follows

$$\eta_{store} = \frac{E_{stored}}{E_{output}} \tag{6}$$

where E_{output} is the maximum energy output as mentioned earlier and E_{stored} indicates the energy that can be effectively stored. The output energy from TENG is generally stored in capacitors or other energy storage units, and the amount of energy stored is determined by the energy storage efficiency. Because of the variation of equivalent capacitor value, the output voltage of TENG has an opposite relationship to the output charge with the increasing number of inner segments, which can be theoretically derived as plotted in Figure 4f. However, for most energy storage units, the operation voltage is relatively low compared with the output voltage of TENG. In this case, if the TENG with high output voltage is connected with the storage unit, a small amount of energy will be transferred to the unit, resulting in a low efficiency. As a result, the output voltage of TENG should be lowered to the same level as the operation voltage of storage units, leading to the maximized output charges. The schematic diagram is illustrated in Figure 4f, where the dashed area indicates the maximum energy output of TENG and the shadow zones indicate the maximum energy that can be stored in the storage unit. The dashed area increases from state (i) to state (iii), showing the increased maximum energy output of TENG. During each state, a certain voltage value can be referred to as an operation value of the energy storage; when the output voltage of TENG is above that value, the output charges are limited. Detailed theoretical calculation is provided in Figures S6 and S7 in the Supplementary Information.

Based on the determined inner structure, other factors such as oscillation frequency, amplitude, and dielectric materials were further studied. As demonstrated in **Figure 5**a,b, the output voltage and current for both TENG and EMG under a wide frequency range were achieved by two working modes: a shaking mode providing low-frequency oscillation driven by a shaker and a shifting mode providing relatively high-frequency oscillation driven by a linear motor. For TENG, V_{oc} gradually decreases as the platform working frequency increases in the two working modes, while I_{sc} generally exhibits a reverse trend with the increasing platform working frequency, except for the sharp drop during the platform switching, which is a result of the reduced transfer charges. Meanwhile, for EMG, both V_{oc} and I_{sc} exhibit a similar linearly upward trend with the increasing platform working frequency in each working mode, but this upward trend varies with the change of working mode because of an extra vertical component of acceleration for the magnets in the shaking mode. The driving frequency generally has an important effect on the output performance of nanogenerator, by changing the flow rate of charges in TENG and the velocity of magnet in EMG. Additionally, the total quantity of triboelectric charges is also influenced by the frequency through the alteration of effective contact area, especially in the low-frequency range. The effective contact area, on the other hand, can be changed by the variation of amplitude in the shaking mode, resulting in the different output performances.
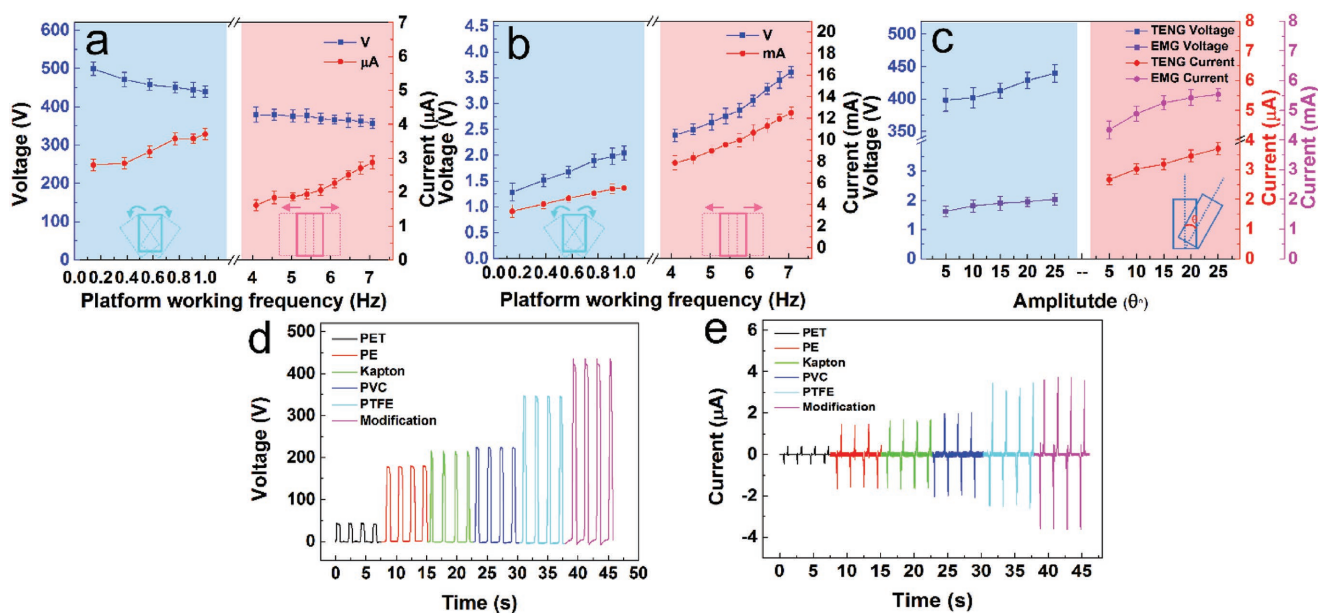
Figure 5. Factors that influence the electric output of hybrid nanogenerator. V_{oc} and I_{sc} of a) TENG and b) EMG vs the platform working frequency under both shaking mode (left) and shifting mode (right). c) V_{oc} and I_{sc} of TENG and EMG vs the amplitude under shaking mode at a driving frequency of 1 Hz. d,e) V_{oc} and I_{sc} of TENGs fabricated with different dielectric materials.

As demonstrated in Figure 5c, the variation of amplitude is represented by the swing angle, which is the angle between the center lines of the device at the original position and the position of maximum amplitude. It is well observed that the V_{oc} and I_{sc} curves of both TENG and EMG move up with the increasing amplitude, indicating that the amplitude plays a positive role in improving the output performance. Specifically, the improved output of TENG is attributed to the increased effective contact area under a wide swing angle, while that of EMG is because of the enhanced velocity component in the direction through the coil. Also, regarding the effect of triboelectric charge on the output of TENG, different dielectric materials were employed for further comparison. Figure 5d,e shows the electrical output of TENG with different materials, i.e., polyethylene terephthalate, polyethylene, Kapton, polyvinyl chloride (PVC), PTFE, and PTFE after modification. Overall, the values of V_{oc} and I_{sc} for different materials basically reflect the ability of triboelectric charge generation, which is consistent with the electron affinity of these materials. The PTFE after modification can produce more triboelectric charge by the enhancement of surface roughness.

To further explore and compare the overall energy output capability for TENG and EMG, the average output powers over a broad frequency range were collected and calculated by connecting to external loads through a rectifier. The arrays of light-emitting diodes (LEDs) were employed as the external load for visual comparison. Of these, 60 blue LEDs were connected in series, while 50 green LEDs were connected in parallel, with the circuit diagram shown in Figure S8 in the Supporting Information. Notably, the total power consumption values for the 60 blue LEDs and the 50 green ones were basically equal due to the individual different resistances. **Figure 6**b shows the average output power of TENG and EMG collected from two platforms, and Figure 6a,c displays the different brightness

of LEDs under the corresponding frequency. The brightness of LED arrays is in accordance with the curves calculated by the collected signals. It is clearly observed that the TENG produces a higher output than the EMG in the shaker platform (<1 Hz), indicating that the energy conversion of TENG is more efficient than that of EMG in the low-frequency range. More importantly, the external load for TENG was constituted by the series LED arrays, whose resistance value is far away from the optimized resistance value (≈100 MΩ). However, the average output power of TENG is ten times that of EMG. The brightness contrast of LEDs can also reflect the different output powers as shown in Figure 6a. The brightness of LEDs intensified as the frequency increased, and the blue LEDs were apparently brighter than the green ones.

Once switching to the linear motor platform, the average output power for EMG increases rapidly, while the growth rate for TENG increases slightly; the two curves thus intersected at a frequency of 5.75 Hz. We define the threshold frequency (f_{th}) as the frequency at which the average output powers for TENG and EMG are equal, and the whole frequency range can be divided into the TENG-dominant range (below f_{th}) and EMG-dominant range (above f_{th}). When the frequency increases to the EMG-dominant range, the output power of EMG is higher than that of TENG, and the green LEDs have more brightness than the blue ones (Figure 6c).

The reason that the energy conversion efficiencies for TENG and EMG varied with different frequency domains can be attributed to their intrinsic characteristics. Specifically, the TENG produces the output power by the transfer of almost unchanged triboelectric charges and maintains a high voltage due to the high electric potentials caused by the triboelectric charges. The frequency therefore mainly affects the flow rate of these charges, and the output power is limited by the current value. However, the limited current value at low
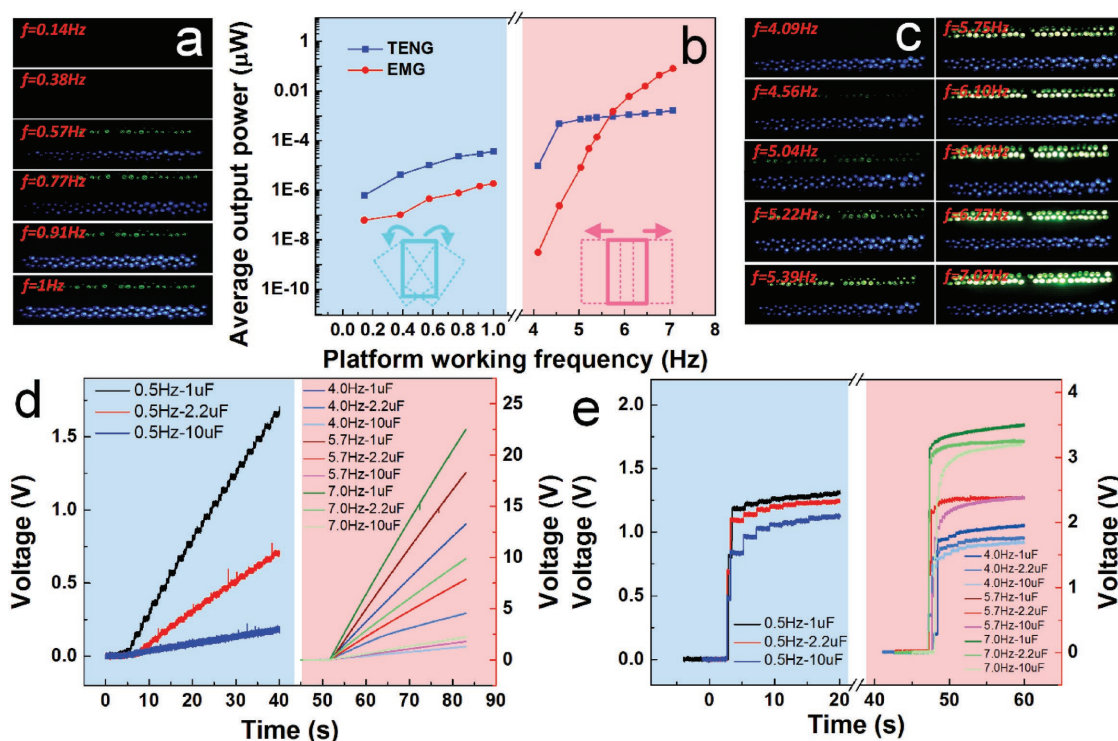
Figure 6. Overall energy output capabilities for TENG and EMG. Photographs of LED arrays supplied by TENG and EMG under a) shaking mode and c) shifting mode. b) The average output powers for both TENG and EMG under varied platform working frequencies with LED loads. Charging performances of d) TENG and e) EMG for various capacitors under varied platform working frequencies.

frequency can be compensated by generating more triboelectric charges, thus improving the output power. This unique feature of TENG can also benefit the output power when connecting with a high-resistance load. On the contrary, the EMG generates the output power by the electromotive force, whose value entirely relies on the frequency. Both voltage and current remain at a low level at the low-frequency range, leading to a very low output power. When the TENG and EMG were connected to external load through a rectifier, a certain voltage drop (0.3–0.8 V) should also be considered. For TENG, this voltage drop is negligible compared with its high voltage output, resulting in a very little energy loss. However, for the EMG as a low-voltage generator, this relatively high voltage drop would largely increase the energy loss, especially in the low-frequency range.

The different overall energy output capabilities for TENG and EMG have also been demonstrated by charging capacitors under various frequencies (Figure 6d,e). While charging the capacitors by TENG through rectifier, the voltage of the capacitor can be charged up to the maximum open-circuit voltage, which is about 400 V in our case. The charging rate is positively correlated with the operation frequency, while has a negative correlation with the capacitance value (Figure 6d). However, for the EMG, the voltage of the capacitor will be rapidly charged up to a saturation value, which is limited by the low open-circuit voltage. Due to the high current, the charging rate remains almost the same regardless of the alterations of operation frequency and capacitance value. The increasing operation frequency can only influence the saturation voltage by improving

the open-circuit voltage of EMG. Notably, the saturation voltage for capacitance values varied slightly at the same frequency, which is a result of various voltage drops for different capacitors. Because of the low saturation voltage, most energy from the EMG cannot be stored and is largely lost, leading to more energy loss compared with TENG.

To demonstrate the performance of hybrid nanogenerator for large-scale blue energy harvesting, the device was full packaged in an acrylic shell and installed on one side of a wing-structure bracket. For the experimental demonstration, a water wave simulation platform consisting of a homemade water tank and a linear motor was employed. As shown in **Figure 7**a, an acrylic plate anchored at the end of the linear motor was used to push the water, and the water waves with different frequencies can be achieved by adjusting the velocity of linear motor. Herein, typical electrical signals for both TENG and EMG were collected under a wave frequency of ≈1 Hz (Figure 7d–h). For TENG, a V_{oc} of 400 V and maximum I_{sc} of 15.3 µA have been reached on the simulated water wave, while the EMG can output a V_{oc} of 1.7 V and an I_{sc} of 5.4 mA. The charging characteristics for TENG, EMG, and hybrid nanogenerator were obtained at different wave frequencies by using a capacitor of 10 µF, and the charging voltage curves are plotted in Figure 7i, suggesting that the charging characteristics for TENG and EMG heavily depend on their inherent features. The hybrid nanogenerator with the integrated features can charge the capacitor in two processes, providing not only high charging voltage, but also rapid charging rate. Initially, the capacitor was rapidly charged up to the saturation voltage determined by EMG, and then gradually
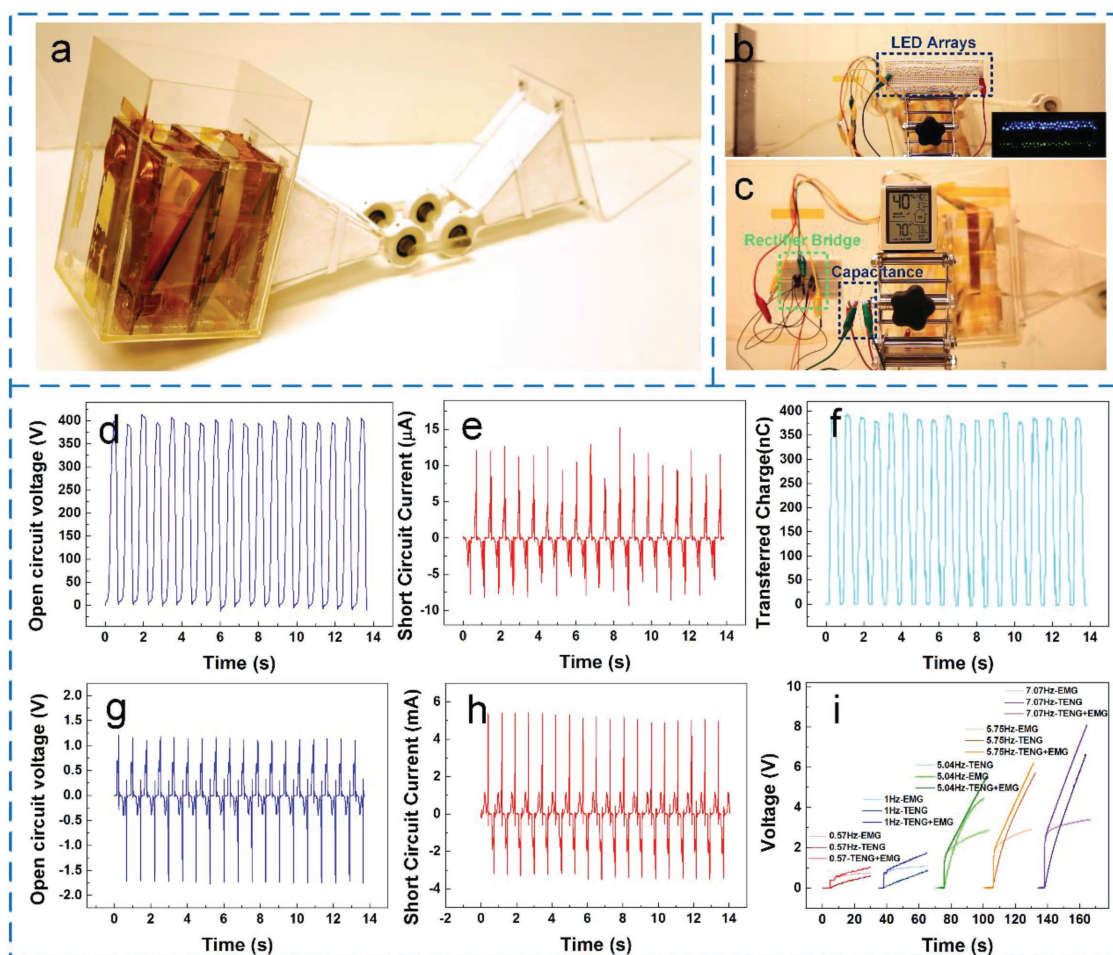
Figure 7. Demonstration of the hybrid nanogenerator as a practical power source under real water environment. a) Photograph of hybrid nanogenerator system with a double-wing structure. Photographs of the hybrid system connected with b) LED arrays directly and c) a thermometer through a rectifier. Electric measurements such as d) V_{oc}, e) I_{sc}, and f) Q_{sc} of TENG, and g) V_{oc} and h) I_{sc} of EMG in a real water environment at a wave frequency of ≈1 Hz. i) Charging performances of TENG, EMG, and hybrid nanogenerator for a capacitor of 10 µF at different water wave frequencies controlled by different driving forces.

charged up to the maximum voltage of TENG. The saturation voltage values in the first stage and the charging rates in the second stage were both increased by the increasing frequency of water waves (Figure 7i). Finally, we demonstrate two applications for the hybrid nanogenerator to supply electricity for LED arrays and a thermometer. In the first demo, 50 green LEDs in parallel were connected to the EMG part and 60 blue ones were connected to the TENG part. The observed lighting of LEDs in the video indicates the stable electrical output for both parts under the water wave (Figure 7b; Video S1 in the Supporting Information). In the second demo, the output of each part is rectified and then connected together in parallel to charge a capacitor of 100 µF; the thermometer started to work to display the right room temperature when the voltage of capacitor increased to about 1.5 V (Figure 7c; Video S2 in the Supporting Information). Furthermore, with the flexible coupling structure, the proposed device can be easily linked together to form a nanogenerator network, which exhibits an effective and sustainable potential for large-scale blue energy harvesting in the future.

3. Conclusion

In summary, a hybrid TENG and EMG nanogenerator system based on an optimized cubic structured unit has been demonstrated for water wave harvesting. The TENG consisting of etched PTFE films and Cu electrodes is designed into cubic structure, in which the contact-freestanding mode is first utilized to solve the existing difficulties and enhance the efficiency of energy harvesting. Meanwhile, the EMG consisting of two pairs of magnets and coils is well hybridized. By integrating the complementary output characteristics of TENG and EMG, the hybrid system is able to deliver a satisfactory output in a broad range of operation frequency. The device with four inner chambers was initially determined by comparing the output performances of optional designs. After that, the effects of oscillation frequency, amplitude, and dielectric materials that influence the output performances of TENG and EMG were studied based on different platforms (shaker and linear motor). Furthermore, the overall energy output capabilities for TENG and EMG were demonstrated through calculated average output powers and

capacitors' charging analysis. As a result, the optimum operation frequency ranges for TENG and EMG were concluded and the hybrid charging strategy was proposed. Finally, the packaged hybrid nanogenerator was demonstrated to harvest simulated water wave energy to simultaneously drive LEDs directly and a thermometer through a rectifying circuit. With the flexible coupling structure, the fabricated hybrid nanogenerator renders an effective and sustainable progress in the practical applications of large-scale blue energy harvesting over a broad frequency range

4. Experimental Section

Modification of PTFE Film and Cu Electrode: The surfaces of Cu electrode and PTFE film were modified by electro-erosion and plasma-etching methods, respectively, to increase surface roughness and the triboelectric charges.

For Cu electrode, the electrochemical erosion was conducted under the electrodischarge platform. Cu foils (100 µm in thickness) were first cut into rectangular samples and then rinsed in water followed by ethanol. The treated samples were placed in the discharge fixture that was immersed in the 0.5 mol L^{-1} $CuSO_4$ solution. The ends of Cu sample were clamped by metal clips that were connected in parallel with the anode and cathode of the power supply. The electrochemical erosion with a constant current density of 20 mA cm^{-2} was applied on the surface of Cu sample for 30 min, and the applied voltage ranged from 0.535 to 0.659 V. After that, the well-modified Cu samples without impurities were selected according to the results of XRD patterns.

The PTFE films (50 µm in thickness) were placed in plasma instrument (Smart Plasma 10 of Germany Plasma Technology) chamber and engraved by 400 W, 40 kHz air plasma for 10 min. After that, the treated samples were ultrasonically cleaned with deionized water and ethanol successively, and dried in a drying oven.

Fabrication of TENG: The TENG is composed of two parts: an acrylic box and four shakable boards. For the acrylic box, a laser cutter (PLS6.75, Universal Laser Systems) was employed to cut 1/8 in. thick acrylic sheets into rectangular shapes with different dimensions as the walls of the acrylic box (4.5 in. × 5 in., 4.5 in. × 6.5 in., and 5 in. × 6.5 in.). The margins of these processed sheets were cut into bulges and trenches for easy assembling. The acrylic box used as the shell of TENG was divided into four separate chambers by three acrylic clapboards with the same thickness. Two of them were used as slopes with the dimensions of 4.25 in. × 6 in., and the other one was used as the vertical baffle with the dimensions of 4.5 in. × 6.5 in. The as-prepared Cu foils were attached on the internal walls of each chamber as the electrodes. Meanwhile, the as-prepared PTFE films were covered on the four shakable boards that were also cut from a 1/16 in. thick acrylic sheet with the same dimension. One edge of the shakable board was fixed at the roof of each chamber by attached flexible films (PVC films with 100/200 µm thickness), making the board freestanding and allowing easy contact with the walls of chambers. Copper wires were used to parallelly connect all the electrodes in four chambers as two terminals according to the contact status between PTFE film and Cu electrodes under oscillations.

Fabrication of EMG: The EMG was composed of two pairs of magnets and two pairs of copper coils. Before attaching the PTFE films, two pairs of NdFeB permanent disk magnets (1 in. diameter and 1/16 in. thickness) were embedded in the shakable boards that belong to the one of the outermost chambers by cutting holes in the boards. Two pairs of copper synclastic twined coils (outer diameter of 4.5 cm and inner diameter of 1 cm) were attached on the left and right sides of the box, with their centers aligned in line with the centers of the magnets, when the shakable board contact with the walls of box. The adjacent magnets were arranged in the same magnetic polarizations and the adjacent coils were also placed in the same winding directions. Copper wires were used to connect the coils in series to produce EMG output.

Assembling of the Hybrid Nanogenerator System: The hybrid system was designed in a double-wing structure, which consisted of two coupled hybrid nanogenerator units and one pivot hinge as a center of the link. Each unit was first fully packaged in an acrylic box and then supported on a bracket. The bracket was connected by two cantilever beams that were anchored on the bearing support in the pivot hinge. Four shielded bearing supports (outer diameter of 4.5 cm and inner diameter of 1.5 cm) were installed on a square ring to constitute the pivot hinge. The bracket, the cantilever beams, and the square ring were all made up of PVC for the light weight. In addition, the pivot hinge was floated on water with polyfoam so that the nanogenerator could operate parallel to the wave direction and effectively ride the waves.

Electrical Measurement: The typical electrical signals of the hybrid nanogenerator were acquired via Keithley 6514 system electrometer. The software platform was constructed based on LabVIEW, which is capable of realizing real-time data acquisition control and analysis.

Supporting Information

Supporting Information is available from the Wiley Online Library or from the author.

Conflict of Interest

The authors declare no conflict of interest.

[1] D. Gielen, F. Boshell, D. Saygin, *Nat. Mater.* **2016**, *15*, 117.
[2] M. Jacobson, M. Delucchi, G. Bazouin, Z. Bauer, C. Heavey, E. Fisher, S. Morris, D. Piekutowski, T. Vencill, T. Yeskoo, *Energy Environ. Sci.* **2015**, *8*, 2093.
[3] Q. Schiermeier, J. Tollefson, T. Scully, A. Witze, O. Morton, *Nature* **2008**, *454*, 816.
[4] Z. L. Wang, *Nature* **2017**, *542*, 159.
[5] Z. L. Wang, T. Jiang, L. Xu, *Nano Energy* **2017**, *39*, 9.
[6] B. Drew, A. Plummer, M. Sahinkaya, *Proc. Inst. Mech. Eng., Part A* **2009**, *223*, 887.
[7] A. Falcao, *Renewable Sustainable Energy Rev.* **2010**, *14*, 899.
[8] J. Scruggs, P. Jacob, *Science* **2009**, *323*, 1176.
[9] Z. L. Wang, *ACS Nano* **2013**, *7*, 9533.
[10] Z. L. Wang, J. Chen, L. Lin, *Energy Environ. Sci.* **2015**, *8*, 2250.

[11] G. Zhu, B. Peng, J. Chen, Q. Jing, Z. L. Wang, *Nano Energy* **2015**, *14*, 126.

[12] Z. L. Wang, *Mater. Today* **2017**, *20*, 74.

[13] L. Pan, J. Wang, P. Wang, R. Gao, Y. Wang, X. Zhang, J. Zou, Z. L. Wang, *Nano Res.* **2018**, *11*, 4062.

[14] J. Wang, W. Ding, L. Pan, C. Wu, H. Yu, L. Yang, R. Liao, Z. L. Wang, *ACS Nano* **2018**, *12*, 3954.

[15] C. Wu, R. Liu, J. Wang, Y. Zi, L. Lin, Z. L. Wang, *Nano Energy* **2017**, *32*, 287.

[16] W. Yang, J. Chen, Q. Jing, J. Yang, X. Wen, Y. Su, G. Zhu, P. Bai, Z. L. Wang, *Adv. Funct. Mater.* **2014**, *24*, 4090.

[17] J. Wang, S. Li, F. Yi, Y. Zi, J. Lin, X. Wang, Y. Xu, Z. L. Wang, *Nat. Commun.* **2016**, *7*, 12744.

[18] G. Zhu, P. Bai, J. Chen, Z. L. Wang, *Nano Energy* **2013**, *2*, 688.

[19] H. Zhang, Y. Yang, T. Hou, Y. Su, C. Hu, Z. L. Wang, *Nano Energy* **2013**, *2*, 1019.

[20] Q. Hua, J. Sun, H. Liu, R. Bao, R. Yu, J. Zhai, C. Pan, Z. L. Wang, *Nat. Commun.* **2018**, *9*, 244.

[21] T. Jiang, Y. Yao, L. Xu, L. Zhang, T. Xiao, Z. L. Wang, *Nano Energy* **2017**, *31*, 560.

[22] Z. Wen, H. Guo, Y. Zi, M. Yeh, X. Wang, J. Deng, J. Wang, S. Li, C. Hu, L. Zhu, Z. L. Wang, *ACS Nano* **2016**, *10*, 6526.

[23] L. Xu, Y. Pang, C. Zhang, T. Jiang, X. Chen, J. Luo, W. Tang, X. Cao, Z. L. Wang, *Nano Energy* **2017**, *31*, 351.

[24] Y. Xi, J. Wang, Y. Zi, X. Li, C. Han, X. Cao, C. Hu, Z. L. Wang, *Nano Energy* **2017**, *38*, 101.

[25] L. Xu, T. Jiang, P. Lin, J. Shao, C. He, W. Zhong, X. Chen, Z. L. Wang, *ACS Nano* **2018**, *12*, 1849.

[26] X. Wang, S. Niu, Y. Yin, F. Yi, Z. You, Z. L. Wang, *Adv. Energy Mater.* **2015**, *5*, 1501467.

[27] S. Zhang, M. Xu, C. Zhang, Y. Wang, H. Zou, X. He, Z. J. Wang, Z. L. Wang, *Nano Energy* **2018**, *48*, 421.

[28] Q. Shi, H. Wang, H. Wu, C. Lee, *Nano Energy* **2017**, *40*, 203.

[29] L. Feng, G. Liu, H. Guo, Q. Tang, X. Pu, J. Chen, X. Wang, Y. Xi, C. Hu, *Nano Energy* **2018**, *47*, 217.

[30] D. Kim, H. Kim, D. Kong, M. Choi, H. Kim, J. Lee, G. Murillo, M. Lee, S. Kim, J. Jung, *Nano Energy* **2018**, *45*, 247.

[31] H. Zhang, Y. Yang, Y. Su, J. Chen, K. Adams, S. Lee, C. Hu, Z. L. Wang, *Adv. Funct. Mater.* **2014**, *24*, 1401.

[32] F. Yi, L. Lin, S. Niu, J. Yang, W. Wu, S. Wang, Q. Liao, Y. Zhang, Z. L. Wang, *Adv. Funct. Mater.* **2014**, *24*, 7488.

[33] Y. Yang, H. Zhang, R. Liu, X. Wen, T. Hou, Z. L. Wang, *Adv. Energy Mater.* **2013**, *3*, 1563.

[34] S. Niu, Y. Liu, S. Wang, L. Lin, Y. Zhou, Y. Hu, Z. L. Wang, *Adv. Funct. Mater.* **2014**, *24*, 3332.

[35] X. Wang, Z. Wen, H. Guo, C. Wu, X. He, L. Lin, X. Cao, Z. L. Wang, *ACS Nano* **2016**, *10*, 11369.

[36] P. Wang, R. Liu, W. Ding, P. Zhang, L. Pan, G. Dai, H. Zou, K. Dong, C. Xu, Z. L. Wang, *Adv. Funct. Mater.* **2018**, *28*, 1705808.

[37] Y. Zi, H. Guo, Z. Wen, M. Yeh, C. Hu, Z. L. Wang, *ACS Nano* **2016**, *10*, 4797.